Multimodal Stochastic Characterization of Subsurface Angle Gathers with Applications to Diffraction Imaging of Karsts

Musa Maharramov, Bin Yu, Victor Lopez, and Min Zhou, Sinopec Tech Houston*

SUMMARY

We propose a data processing method for statistical characterization and classification of subsurface-domain common-image angle gathers. Our approach enables the automatic separation of subsurface image gathers into components from diffractions and specular reflections, aiding in the imaging of relevant geologic features. A key innovation in our method is the statistical modeling of subsurface angle gather attributes using multimodal Gaussian mixture models, which naturally separate scattering patterns. In contrast, traditional deterministic methods, while effective, often require extensive parameter tuning by expert users or impose stricter requirements on input gather generation, such as maintaining high amplitude fidelity. Similarly, high-capacity statistical models like neural networks demand significant data collection, training, and fine-tuning of inherently black-box models. We illustrate the effectiveness of our methodology with a land field-data application, using our diffraction separation technique to image carbonate karst caves.

INTRODUCTION

Diffraction imaging provides critical complementary information to reflections, particularly in complex geologic settings (Klem-Musatov, 1994). It has proved valuable in deep subsalt regions (Foss et al., 2018), delineating fault surfaces and locations (Ogiesoba et al., 2015; Protasov et al., 2021), and improving the prediction and visualization of hydraulically conductive fractures (Burnett et al., 2015; Duan et al., 2017; Protasov et al., 2021). Our goal is to develop a highly autonomous and computationally efficient method for separating multi-azimuth dip gathers into diffraction and specular reflection components, minimizing the need for user-driven parameter adjustments while reducing strict amplitude fidelity requirements for the input gathers.

In the following, $G = G(\mathbf{x}_I, \alpha, \delta)$ denotes a multi-azimuth dip gather, where $\mathbf{x}_I = (x^1, x^2, x^3)$ is a subsurface image point, $\alpha \in [0, 2\pi]$ and $\delta \in [0, \pi/2]$ are the azimuth and dip angles (Xu et al., 2001; Biondi, 2006; Koren and Ravve, 2011; Ravve and Koren, 2011). A diffractor image I_d and its complementary specular reflection image I_r can be generated by partially stacking gathers G,

$$I_d(\mathbf{x}_I, \alpha) = \int_0^{\frac{\pi}{2}} \phi(\mathbf{x}_I, \alpha, \delta) G(\mathbf{x}_I, \alpha, \delta) d\delta, \quad (1)$$

$$I_r(\mathbf{x}_I, \alpha) = \int_0^{\frac{\pi}{2}} [1 - \phi(\mathbf{x}_I, \alpha, \delta)] G(\mathbf{x}_I, \alpha, \delta) d\delta, \quad (2)$$

after applying a filter $\phi(\mathbf{x}_I, \alpha, \delta)$, which selectively isolates diffraction-related scattering from specular reflections. In the subsurface image-point angle-gather domain, specular reflections appear as parabolic curves plotted against the dip, with their apexes located at the correct dip angle (Audebert et al., 2002; Klokov and Fomel, 2012) – see Figure 1. In principle, specular reflections can be removed by eliminating these apexes, or Fresnel zones (for correct migration velocity), while the curved portions of the parabolas cancel each other out (Kozlov et al., 2004; Moser and Howard, 2008; Koren and Ravve, 2011; Decker et al., 2013). Apex selection can be achieved using a specularity filter leveraging contributions from multiple opening angles and azimuths (Koren and Ravve, 2011; Dafni and Symes, 2016a,b,c). However, our methodology conceptually aligns with another common approach to diffraction separation, which is based on dip semblance.

When the migration velocity is correct, summing all angle gathers over all dip angles produces a focused image, as predicted by the stationary phase principle (Bleistein et al., 2001). The flatness of dip gathers for diffraction events, or *dip semblance*, can serve as an indicator of migration velocity accuracy in diffraction velocity analysis (Decker et al., 2017). Dip semblance can be used as a weighting function or filter ϕ applied to the angle gathers in equation 1 to form a diffraction image. In this work, we propose a probabilistic framework for designing a dip filter ϕ that effectively separates diffractions from reflections in equation 1.

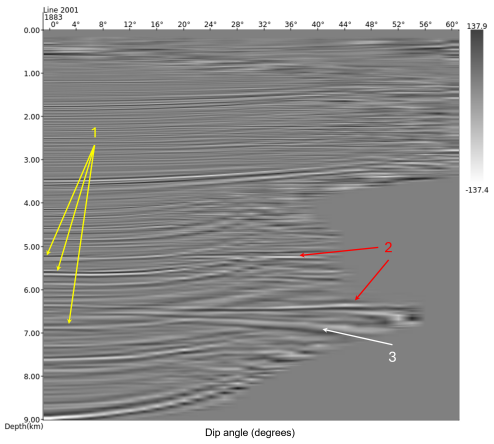

Figure 1: Dip angle gathers from a land seismic survey. Reflectors appear flat over a narrow Fresnel zone of dips centered around the true reflector dip (1), curving away at incorrect dips, while diffractors produce signals that remain flat across a broader range of dips (2). Diffraction events unrelated to the specified image point do not exhibit flatness (3).

Our approach introduces an automated feature extraction method for unweighted gathers G based on statistical analysis of horizontal correlation lengths of dip gathers, treated as statistical attribute fields. This feature extraction extends method-

ologies commonly used in Geostatistics (Grana et al., 2021), treating gather attributes as datasets that reveal geometric similarity patterns. General statistical models, such as the Principal Component Analysis (PCA) and neural networks, have been explored in related contexts (Serfaty et al., 2017; Dell et al., 2020; Dafni et al., 2020). However, our method is distinct in leveraging Gaussian Mixture Models (GMM) to statistically characterize flatness-induced horizontal correlation lengths of gathers G following their expansion in a dictionary of scale-dependent wavelets. In this framework, the classification label (specular reflection versus diffraction) becomes a discrete latent variable inferred using the Expectation-Maximization (EM) algorithm, where diffractor labeling is iteratively refined through alternating optimization of discrete and continuous latent attributes. The diffraction-related modes of the resulting mixture distribution are used similarly to dip semblance, serving as classification-dependent filters to separate diffractions from specular reflections.

THEORY

In our methodology, each subsurface image point $\mathbf{x}_I$, azimuth α and dip angle δ are associated with two key attributes: the gather correlation length along the dip axis, $\lambda = \lambda(\mathbf{x}_I, \alpha, \delta)$, and a discrete scattering type, $\nu = \nu(\lambda(\mathbf{x}_I, \alpha, \delta))$. As we will discuss later, the distribution of correlation lengths λ is modeled as a multimodal probability distribution. Our approach focuses on identifying and separating the modes of this distribution, distinguishing those corresponding to diffractions from those associated with specular reflections.

This task is made computationally tractable by representing the distribution as a mixture distribution marginalized over the latent variable ν (Bishop, 2024),

$$p(\lambda;\mathbf{g}) = \sum_{\nu} p(\lambda|\nu;\mathbf{g})p(\nu;\mathbf{g}), \tag{3}$$

where $\mathbf{g}$ denotes model parameters (or "hyperparameters"); $\mathbf{g}$ may be omitted in some equations for simplicity.

After substituting computationally tractable forms for the distributions on the right-hand side of equation 3, we perform iterative estimation of mixture hyperparameters using the "Expectation-Maximization" (EM) algorithm (Dempster et al., 1977; Hastie et al., 2008; Bishop, 2024). The primary output of the process is the posterior probability distribution of class labels $p(\nu|\lambda = \lambda(\mathbf{x}_I, \alpha, \delta))$, which is then used to estimate the diffractor and specular reflector images via modified versions of equations 1 and 2,

$$\mathbb{E}\left[I_d^k\right](\mathbf{x}_I, \alpha) = \int_0^{\frac{\pi}{2}} p(\nu = k|\lambda(\mathbf{x}_I, \alpha, \delta))G(\mathbf{x}_I, \alpha, \delta)d\delta, \tag{4}$$

$$\mathbb{E}\left[I_r\right](\mathbf{x}_I, \alpha) = \int_0^{\frac{\pi}{2}} p(\nu = 0|\lambda(\mathbf{x}_I, \alpha, \delta))G(\mathbf{x}_I, \alpha, \delta)d\delta. \tag{5}$$

In equations 4 and 5, we assume that $\nu = 0$ represents the specular reflector class label, and $\nu = k = 1, 2, \ldots$ represent potentially multiple diffraction class labels, and the left-hand sides are the mathematical expectations of partial diffraction and specular reflection images, respectively. The presence of multiple diffraction classes reflects the fact that different diffractors may be illuminated over varying angle ranges, depending on their depth and the complexity of the subsurface.

The subsequent discussion outlines key details of our algorithm. We introduce a dictionary of wavelets in the depth domain, $\{r_l(z)\}$, parameterized by a wavelength parameter l. Such wavelets can define, for example, bandpass filters in the wavenumber domain for different wavelengths, determined by the frequency content of input seismic data D. For each member of the wavelet dictionary, we evaluate "gather coherence" of the dip gather G as its correlation with the wavelet for each subsurface image point $\mathbf{x}_I = (x^1, x^2, x^3)$), azimuth α and dip δ,

$$\chi_l(\mathbf{x}_I, \alpha, \delta) \;=\; \mathrm{corr}\left[r_l(z - x^3), G\left(x^1, x^2, z, \alpha, \delta\right)\right], \tag{6}$$

where z is the integration variable. The five-dimensional coherence volume in equation 6 is used to compute a custom quantity that we call "correlation length" for each subsurface image point, azimuth and dip, as a measure of the gathers' flatness for each subsurface location, azimuth and dip angle. We compute mean coherence and horizontal covariance volumes of the coherences 6,

$$\begin{aligned}
&\overline{\chi}_l(\mathbf{x}_I, \alpha, \delta) \;=\; \underset{\varepsilon\in[-\Delta,+\Delta]}{\mathrm{mean}} \chi_l(\mathbf{x}_I, \alpha, \delta + \varepsilon), \\
&C_l(\mathbf{x}_I, \alpha, \delta, \lambda) \;= \\
&\underset{\varepsilon\in[-\Delta,+\Delta]}{\mathrm{mean}} \{\chi_l(\mathbf{x}_I, \alpha, \delta + \varepsilon) - \overline{\chi}_l(\mathbf{x}_I, \alpha, \delta + \varepsilon)\} \times \\
&\{\chi_l(\mathbf{x}_I, \alpha, \delta + \lambda + \varepsilon) - \overline{\chi}_l(\mathbf{x}_I, \alpha, \delta + \lambda + \varepsilon)\},
\end{aligned} \tag{7}$$

with larger positive values of the covariance indicating similar coherence (e.g., flatter gathers) for dip angles δ and $\delta + \lambda$. In an approach similar to Geostatistical methods of estimating spatial correlation of random attribute fields, we fit the covariance volume of equation 7 to the law of exponential decay,

$$\frac{C_l(\mathbf{x}_I, \alpha, \delta, \lambda)}{C_l(\mathbf{x}_I, \alpha, \delta, 0)} \;\sim\; \exp - \frac{\mathrm{const} \cdot \lambda}{\lambda_l(\mathbf{x}_I, \alpha, \delta)} \tag{8}$$

estimating the "correlation length" $\lambda_l(\mathbf{x}_I, \alpha, \delta)$ as a regression parameter. Parameter λ_l in equation 8 is conceptually similar to the correlation length introduced in Geostatistics as a measure of the continuity of a random attribute field in a specific direction (Doyen, 2007; Grana et al., 2021), and in our case is likewise used as a measure of gather flatness along the dip axis – see Figure 1. The core assumption of our methodology is the assumption that the correlation lengths 8 are distributed according to a mixture distribution,

$$\Lambda_l \ni \lambda(\mathbf{x}_I, \alpha, \delta) \sim \sum_{\nu} p(\lambda|\nu)\pi(\nu), \tag{9}$$

where, as in equation 3, ν is a latent variable that defines one of $K \geq 2$ reflector or diffractor classes, $\pi(\nu) = p(\nu)$ is the marginal, or prior, mode (class) probability associated with mode ν. Our objective now is to estimate the class posterior probabilities,

$$p(\nu = i|\lambda = \lambda(\mathbf{x}_I, \alpha, \delta)),\ i = 0, 1, \ldots, K-1 \tag{10}$$

to use in the diffraction and specular reflection image estimations 4,5. We assume that $p(\lambda|\nu), \nu = 0, 1, \ldots, K-1$ are Gaussian distributions, $p(\lambda|\nu = i) = p(\lambda|\nu = i; \mathbf{g}) = \mathcal{N}\left(\lambda|\overline{\lambda}_i; \sigma_i^2\right)$. The means $\overline{\lambda}_i$ and variances σ_i^2 of these Gaussian distributions, along with the marginal class probabilities $\pi(\nu)$, are statistical model hyperparameters, $\overline{\lambda}_i, \sigma_i^2, \pi(\nu = i) \in \mathbf{g}$, $i = 0, 1, \ldots, K-1$. We generate histograms for one-dimensional sets of correlation lengths Λ_l, shown in Figures 2a,2b for two scales. We subsequently approximate the generated histograms with Gaussian mixtures 9 using the Expectation Maximization algorithm. Once the mixture hyparameters have been estimated, we use Bayes' rule to compute the posterior class probabilities

$$p(\nu = i|\lambda) = \frac{p(\lambda|\nu = i)\,\pi(\nu = i)}{\sum_{j=0}^{K-1} p(\lambda|\nu = j)\,\pi(\nu = j)}, \qquad (11)$$

and substitute them into the image formation equations 4,5. Scattering from variably illuminated diffractors may contribute to the same, albeit skewed, mode – as can bee seen in Figures 2a and 2b. Some mode skewness may result from weaker diffractions associated with slightly different imaging dip ranges. Unless these diffractions are resolved into separate dedicated modes in the density mixture, their scattering contributions may be misclassified as belonging to the tail of an existing mode in equation 9, potentially compromising the fidelity of the diffraction image. Using a larger K (set to 10 in our field-data experiments discussed in the next section) enables us to capture these weaker modes, which, after normalization by the marginal class probability $\pi(\nu)$, contribute physically meaningful amplitudes to the diffraction image in equation 4. This approach effectively replaces a single dip-semblance filter of equation 1 with $K-1$ distinct filters, each selected based on the classification of local gather correlation lengths.

RESULTS AND DISCUSSION

To evaluate the effectiveness of our methodology, we applied it to field data from a land survey characterized by complex subsurface geology. The study area contains an igneous rock layer overlaying a salt body, beneath which lie subsalt carbonate formations. The primary imaging targets are karst caves within the carbonate layer, which often cluster around and connect via hydraulically conductive faults. These caves, filled with hydrocarbons, vary in size – sometimes measuring just tens of meters – making their detection particularly challenging. Compounding the difficulty is the significant seismic velocity contrast at the igneous and salt interfaces, which complicates conventional imaging techniques.

For this experiment, full-stack images and angle gathers G were generated using Kirchhoff migration with a tomographically derived acoustic velocity model. We present two pair of images, each consisting of a conventional full-stack image and the corresponding diffraction image. The images illustrate how diffractors, which are either indistinct or barely perceptible in the full stack, stand out sharply against a nearly empty background in the diffraction image – demonstrating the power of the proposed stochastic filter. The constant-crossline cross-sections of Figures 3a,3b highlight point diffractors that are otherwise uninterpretable or indirectly inferred in the full-stack image, such as through apparent reflector discontinuities. The constant-depth cross-sections of Figures 4a,4b further demonstrate the enhanced interpretability of the spatial distribution and clustering of point diffractors.

We propose a novel methodology for diffraction imaging that operates on unprocessed, unweighted angle gathers, which can be generated using a standard and widely available Kirchhoff migration algorithm. By leveraging Geostatistical random attribute field classification techniques applied directly to artifact-contaminated dip angle gathers, our approach minimizes parameterization and preprocessing burden on the user. While it broadly aligns with dip-filtering methodologies, its statistically derived, context-dependent multiple filter selection shows the potential for enhanced resolution and robustness. Additionally, its ability to isolate and classify weak diffractions under variable illumination makes it a valuable tool for interpretative imaging.

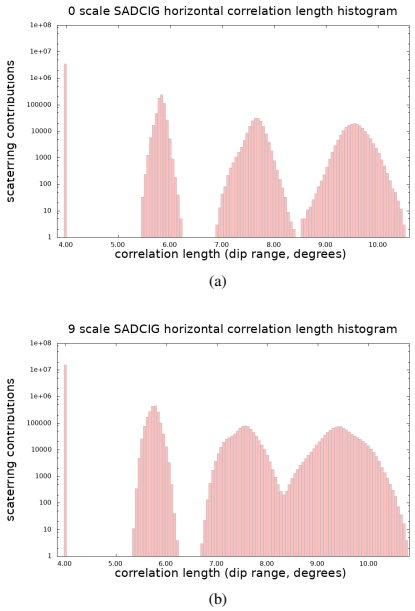

Figure 2: Logarithmic-scale histograms of the correlation length datasets Λ_l, excluding the dominant mode at $\lambda = 0$: (a) $l = 0$ corresponding to vertical wavenumber scale of 0-5% of Nyquist (b) $l = 9$ corresponding to 45-50% of Nyquist. Note the relative increase in the density of diffractions at the shorter wavelength, reflecting the prevalence of smaller diffractors in the acquisition.

ACKNOWLEDGMENTS

The authors would like to thank Dr. Changhua Zhang and Dr. Mingqiu Luo for a number of fruitful discussions, Xibei Oil Field for supporting the field-data experiments, and Sinopec Tech Houston for the permission to publish this work.

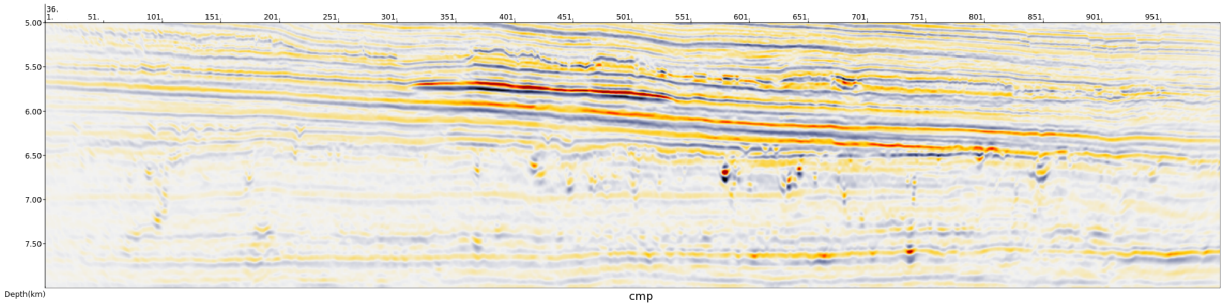

(a)

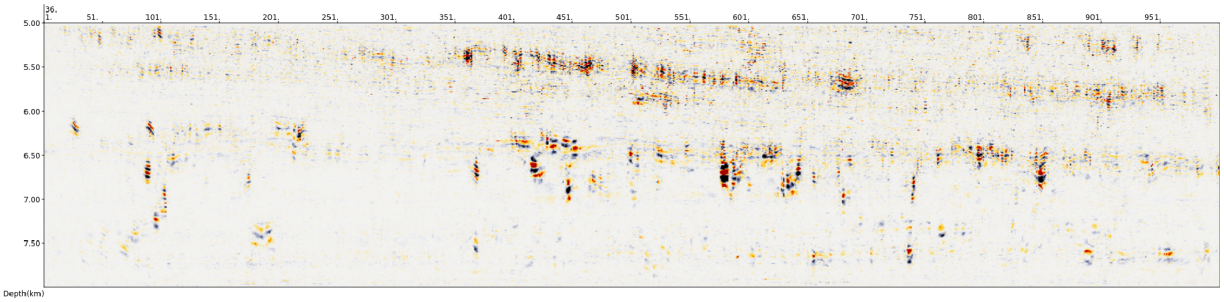

(b)

Figure 3: A single in-line full stack (a) and diffractor image (b) for land field data. The diffraction image reveals both strong and weak diffractors that predominantly represent karst caves in the lower carbonate layer.

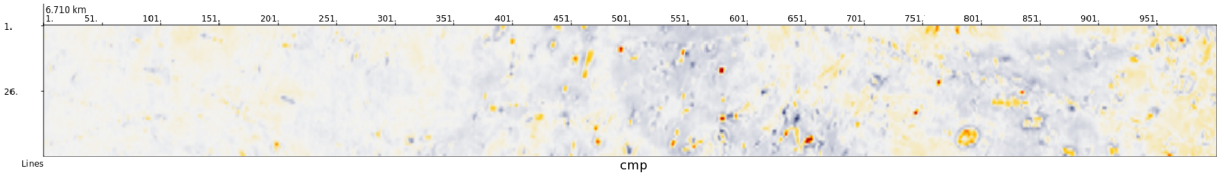

(a)

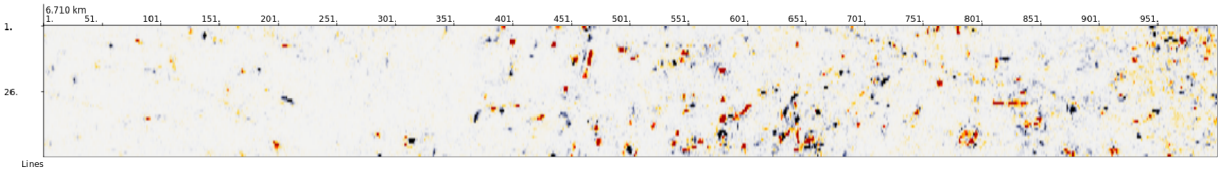

(b)

Figure 4: A single depth slice of the full stack (a) and diffractor image (b) for land field data. Point-diffractors of variable scale (e.g., karst caves) are detectable by energy scattered in a wide range of azimuths.

REFERENCES

Audebert, F., P. Froidevaux, H. Rakotoarisoa, and J. Svay-Lucas, 2002, Insights into migration in the angle domain: SEG Technical Program Expanded Abstracts 2002, 1188–1191.

Biondi, B. L., 2006, 3D seismic imaging: SEG.

Bishop, C. M., 2024, Deep learning: Foundations and concepts: Springer.

Bleistein, N., J. W. Stockwell, and J. K. Cohen, 2001, Mathematics of multidimensional seismic imaging, migration, and inversion: Springer.

Burnett, W. A., A. Klokov, S. Fomel, R. Bansal, E. Liu, and T. Jenkinson, 2015, Seismic diffraction interpretation at Piceance Creek: Interpretation, **3**, no. 1, SF1–SF14. (doi:10.1190/INT-2014-0091.1).

Dafni, R., R. Schwartz, R. Levy, and Z. Koren, 2020, Using principal component analysis to decouple seismic diffractions from specular reflections: SEG Technical Program Expanded Abstracts 2020, 2958–2962. (doi:10.1190/segam2020-3421255.1).

Dafni, R., and W. Symes, 2016a, Dip-angle domain specularity filter design in relation with subsurface offset extended RTM: SEG Technical Program Expanded Abstracts 2016, 4362–4366. (doi:10.1190/segam2016-13820152.1).

Dafni, R., and W. W. Symes, 2016b, Kinematic artifacts in the subsurface-offset extended image and their elimination by a dip-domain specularity filter: GEOPHYSICS, **81**, S477–S495.

———, 2016c, Scattering and dip angle decomposition based on subsurface offset extended wave-equation migration: GEOPHYSICS, **81**, no. 3, S119–S138. (doi:10.1190/geo2015-0528.1).

Decker, L., A. Klokov, and S. Fomel, 2013, Comparison of seismic diffraction imaging techniques: Plane wave destruction versus apex destruction: SEG Technical Program Expanded Abstracts 2013, 4054–4059.

Decker, L., D. Merzlikin, and S. Fomel, 2017, Diffraction imaging and time-migration velocity analysis using oriented velocity continuation: GEOPHYSICS, **82**, no. 2, U25–U35. (doi:10.1190/geo2016-0141.1).

Dell, S., J. Walda, A. Hoelker, and D. Gajewski, 2020, Categorizing and correlating diffractivity attributes with seismic-reflection attributes using autoencoder networks: GEOPHYSICS, **85**, no. 4, O59–O70. (doi:10.1190/geo2019-0574.1).

Dempster, A. P., N. M. Laird, and D. B. Rubin, 1977, Maximum likelihood from incomplete data via the EM algorithm: Journal of the Royal Statistical Society. Series B (Methodological), **39**, 1–38.

Doyen, P. M., 2007, Seismic reservoir characterization: an Earth modelling perspective: EAGE.

Duan, W., G. Peng, X. Song, and X. Li, 2017, Local angle domain imaging and fracture prediction in Tarim Basin: SEG Technical Program Expanded Abstracts 2017, 1006–1010. (doi:10.1190/segam2017-17677545.1).

Foss, S.-K., J. L. L. Matias, A. Sollid, L. Loures, T. Pinotti, E. O. Brenne, Ø. Wergeland, T. M. O. Broch, D. Merten, and N. Ettrich, 2018, Examples of geology from seismic diffractions: SEG Technical Program Expanded Abstracts 2018, 4141–4145. (doi:10.1190/segam2018-2996829.1).

Grana, D., T. Mukerji, and P. Doyen, 2021, Seismic reservoir modeling: Theory, Examples, and Algorithms: Wiley Blackwell.

Hastie, T., R. Tibshirani, and J. Friedman, 2008, The elements of statistical learning: data mining, inference, and prediction: Springer.

Klem-Musatov, K., 1994, Theory of seismic diffractions: SEG.

Klokov, A., and S. Fomel, 2012, Separation and imaging of seismic diffractions using migrated dip-angle gathers: GEOPHYSICS, **77**, S131–S143.

Koren, Z., and I. Ravve, 2011, Full-azimuth subsurface angle domain wavefield decomposition and imaging Part I: Directional and reflection image gathers: GEOPHYSICS, **76**, no. 1, S1–S13. (doi:10.1190/1.3511352).

Kozlov, E., N. Barasky, E. Korolev, A. Antonenko, and E. Koshchuk, 2004, Imaging scattering objects masked by specular reflections: SEG Technical Program Expanded Abstracts 2004, 1131–1134.

Moser, T., and C. Howard, 2008, Diffraction imaging in depth: Geophysical Prospecting, **56**, 627–641.

Ogiesoba, O. C., A. Klokov, and R. Hernandez, 2015, Diffraction imaging of polygonal faults within a submarine volcanic terrain, Maverick Basin, south Texas: Interpretation, **3**, no. 1, SF81–SF99. (doi:10.1190/INT-2014-0105.1).

Protasov, M., V. Tcheverda, and V. Shilikov, 2021, 3D diffraction imaging attributes and their application for fault and fracture localization and characterization: Journal of Applied Geophysics, **191**, 104346. (doi:https://doi.org/10.1016/j.jappgeo.2021.104346).

Ravve, I., and Z. Koren, 2011, Full-azimuth subsurface angle domain wavefield decomposition and imaging: Part 2 local angle domain: GEOPHYSICS, **76**, no. 2, S51–S64. (doi:10.1190/1.3549742).

Serfaty, Y., L. Itan, D. Chase, and Z. Koren, 2017, Wavefield separation via principle component analysis and deep learning in the local angle domain: SEG Technical Program Expanded Abstracts 2017, 991–995. (doi:10.1190/segam2017-17676855.1).

Xu, S., H. Chauris, G. Lambar, and M. Noble, 2001, Common–angle migration: A strategy for imaging complex media: GEOPHYSICS, **66**, 1877–1894.